Ocean Engineering 37 (2010) 549–566

Contents lists available at ScienceDirect

Ocean Engineering

journal homepage: www.elsevier.com/locate/oceaneng

Resistance and propulsion characteristics of various commercial ships based on CFD results

J.E. Choi *, K.-S. Min, J.H. Kim, S.B. Lee, H.W. Seo

Hyundai Heavy Industries, 1, Jeonha-dong, Dong-gu, Ulsan 682-792, Republic of Korea

ARTICLE INFO

Article history:
Received 9 January 2009
Accepted 11 February 2010
Available online 24 February 2010

Keywords:
Computational prediction
Speed performance
Resistance
Propulsion
Commercial ship

ABSTRACT

This paper uses computational tools to examine the speed performance of various types of commercial ships including resistance and propulsion characteristics. Eight commercial ships built in the last decade were selected for the study. They include four large-sized container carriers, one bulk carrier, one VLCC, and two LNG carriers. The Reynolds averaged Navier–Stokes equation has been utilized, and the computations were executed under the same conditions of the model tests to predict the speed performance, i.e., resistance and self-propulsion. The self-propulsion point was obtained from load-varying tests. The speed performance was predicted based on the model-ship performance analysis method of the revised ITTC'78 method. The limiting streamlines on the hull, wave characteristics around the model ship, and the wake characteristics on the propeller plane were also investigated. After completing the computations, a series of model tests were conducted to evaluate the accuracy of the computational predictions. The predictions clearly reveal the differences in the resistance and propulsion characteristics regarding the various types of commercial ships, and may be applicable to hull-form design.

1. Introduction

Predicting the speed performance of the various types of hull forms and propellers during the initial designing stage is essential to develop a fuel-efficient hull form. The traditional means of prediction was experimenting. The approach is reliable, but it also consumes extensive time and cost. A computational method has become more available thanks to the rapid advances in numerical analysis and computing power. Other advantages of this method include the fact that the local flow characteristics, which are difficult to obtain in model tests, are more readily obtained.

In the experimental approach, three kinds of model tests are performed in a deep-water towing tank, i.e., resistance, propeller open water, and self-propulsion tests. A self-propulsion point is obtained through either of the two methods (Stenson et al., 1996). The point may be directly acquired by varying either the propeller loading or the towing speed over a small range. This is known as the 'continental method'. The other way is to interpolate the results of the under-/over-loaded propeller conditions for a given speed, also known as the 'load-varying test' (or the 'British method'). The speed performance is analyzed from the ITTC'78 (Lindgren et al., 1978) utilizing the towing force, propeller rotative speed, propeller thrust and the torque at the self-propulsion point. The computational approach predicts the speed performance basically in the same manner (Choi et al., 2009). Making computational predictions requires the computations at towing and self-propulsion conditions corresponding to the resistance and the self-propulsion model tests, respectively. In the case of the towing computation, numerous researches have been conducted recently on the free-surface flow around the ship, and the accuracy has been improving (Kodama, 1994; Park et al., 2004; Hino, 2005; Tahara et al., 2006). In the case of the self-propulsion computation, the flow around the hull with a rotating propeller and a rudder must be analyzed. The flow around the rotating propeller may be predicted directly or indirectly. A direct approach utilizes the viscous-flow solver taking the propeller geometry into consideration (Lübke, 2005). An indirect prediction requires an iterative progress between the viscous- and the potential-flow solver by presuming the propeller to be an actuator disk (Stern et al., 1988; Kawamura et al., 1997; Choi and Kinnas, 2001; Kim et al., 2005; Chao, 2005; Hino, 2006; Tahara et al., 2006; Choi et al., 2009).

This paper examines the speed performances of the eight different commercial ships that have been built in the last decade. Computations were conducted in towing and self-propulsion conditions. In the towing computations, two types of models were used for the treatment free surface, i.e., the double-body and the free-surface model. In the self-propulsion computations, the double-body model was applied. The 'load-varying tests' were used to obtain the self-propulsion point. The revised ITTC'78

* Corresponding author. Tel.: +82 52 202 5540; fax: +82 52 202 3410.
E-mail address: jechoi@hhi.co.kr (J.E. Choi).

0029-8018/$ - see front matter © 2010 Elsevier Ltd. All rights reserved.
doi:10.1016/j.oceaneng.2010.02.007

method was used for the prediction of the speed performance. The Gridgen (2003), the MPUF-3A (Choi and Kinnas, 2003; Lee and Lee, 2004) and the Fluent V6.3 (2008) codes were used for the grid generation, the potential and the viscous-flow solver, respectively. The computations were carried out using the Linux cluster. The runs performed for these works employed up to 15 3.0 GHz Xeon processors, with 2 GB of RAM each. Computing time for the towing conditions applying the double-body and the free-surface model, and the self-propulsion conditions applying the double-body model were 5, 300 and 30 h, respectively. The model tests were conducted in a deep-water towing tank to validate the numerical results.

2. Numerical method

The ship fixed righted-handed global coordinate system (x, y, z) is defined as positive x in the flow direction, positive y in the starboard, and positive z upward, as shown in Fig. 1. The origin is the intersection point of the midship, the centerplane and the undisturbed free surface; while the origin of the local coordinate system (x', y', z') is also defined at the center of the propeller.

The details and the formulations of the numerical methodologies for CFD are well known and extensively documented in many literatures. Hence, only the main features of the methodologies will be described in this paper.

2.1. Governing equation

The governing equations for the incompressible turbulent flow are the instantaneous conservation of mass (continuity equation) and momentum (Reynolds averaged Navier–Stokes, RANS). These equations are expressed in tensor notation as follows:

$$\frac{\partial U_i}{\partial x_i} = 0 \tag{1}$$

$$\rho\frac{\partial U_i}{\partial t} + \rho U_\ell \frac{\partial U_i}{\partial x_\ell} = -\frac{\partial p}{\partial x_i} + \frac{\partial}{\partial x_\ell}\left(\mu\frac{\partial U_i}{\partial x_\ell} - \rho\overline{u_i u_\ell}\right) + f_{bi} \tag{2}$$

where $U_i=(U, V, W)$ is the velocity component in $x_i=(x, y, z)$ direction, while p, ρ, μ, $-\rho\overline{u_i u_\ell}$ and f_{bi} are the static pressure, fluid density, fluid viscosity, Reynolds stresses, and body forces per unit volume, respectively.

2.2. Turbulence model

The Reynolds stresses in Eq. (2) are known to be important for the more accurate flow predictions around a ship, especially in the case of a fuller ship (Hino, 2005; Gorski and Coleman, 2005). The Reynolds stress turbulence model is applied for the turbulence closure.

The Reynolds stresses are expressed as the form of partial differential equation deduced from the Navier–Stokes equation:

$$\frac{D\overline{u_i u_j}}{Dt} = D_{ij} + G_{ij} - \frac{2}{3}\delta_{ij}\varepsilon + PS \tag{3}$$

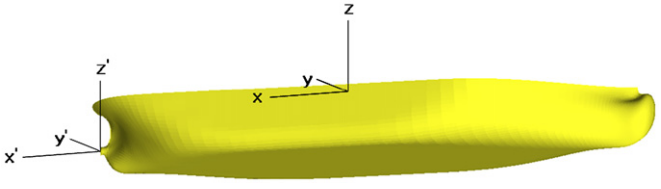

Fig. 1. Coordinate system.

where D_{ij}, G_{ij} and PS are diffusion, generation and the pressure strain term, respectively, and δ_{ij} is the Kronecker delta:

$$D_{ij} = \frac{\partial}{\partial x_\ell}\left(C_k\frac{k^2}{\varepsilon}\frac{\partial\overline{u_i u_j}}{\partial x_\ell} + \nu\frac{\partial\overline{u_i u_j}}{\partial x_\ell}\right) \tag{4}$$

$$G_{ij} = -\left(\overline{u_i u_\ell}\frac{\partial U_j}{\partial x_\ell} + \overline{u_j u_\ell}\frac{\partial U_i}{\partial x_\ell}\right) \tag{5}$$

$$PS = -C_1\frac{\varepsilon}{k}\left(\overline{u_i u_j} - \frac{2}{3}\delta_{ij}k\right) - C_2\left(G_{ij} - \frac{2}{3}\delta_{ij}G_k\right) \tag{6}$$

where $C_k(=0.09)$, $C_1(=1.8)$ and $C_2(=0.6)$ are the turbulence model constants. And k and ε represent turbulent kinetic energy and the dissipation rate of turbulent kinetic energy, respectively:

$$\frac{Dk}{Dt} = \frac{\partial}{\partial x_\ell}\left(C_k\frac{k^2}{\varepsilon}\frac{\partial k}{\partial x_\ell} + \nu\frac{\partial k}{\partial x_\ell}\right) - \overline{u_i u_\ell}\frac{\partial U_i}{\partial x_\ell} - \varepsilon \tag{7}$$

$$\frac{D\varepsilon}{Dt} = \frac{\partial}{\partial x_\ell}\left(C_\varepsilon\frac{k^2}{\varepsilon}\frac{\partial\varepsilon}{\partial x_\ell} + \nu\frac{\partial\varepsilon}{\partial x_\ell}\right) - C_{\varepsilon 1}\frac{\varepsilon}{k}\overline{u_i u_\ell}\frac{\partial U_i}{\partial x_\ell} - C_{\varepsilon 2}\frac{\varepsilon^2}{k} \tag{8}$$

where $C_\varepsilon(=0.07)$, $C_{\varepsilon 1}(=1.44)$, and $C_{\varepsilon 2}(=1.92)$ are the turbulence model constants.

2.3. Source terms of body forces

An asymmetry body-force propeller is applied where the effect of a finite blade number is neglected (Kawamura et al., 1997). The incoming flow velocity on the propeller plane obtained from the RANS solver (Fluent) becomes the input data for the potential-flow solver (MPUF-3A). After getting thrust (T) and torque (Q) distribution acting on an actuator disk and induced velocity from the potential solver, the thrust and torque are substituted for the body forces which are the source terms of RANS. These iterative processes are performed until the thrust and torque converge. User-defined function was used to implement the asymmetry body-force propeller model to the Fluent code.

The axial change of the body force is neglected, i.e., $\vec{f}_b = \vec{f}_b(r,\theta)$. The axial body-force distribution is expressed as in the following equation using thrust and distribution function (I):

$$\iiint_V f_{bx}\,dV = T\iiint_V \frac{I(r_1, r_2; \theta_1, \theta_2)}{\pi(R_P^2 - R_H^2)\Delta x}\,dV \tag{9}$$

or

$$f_{bx} = T\frac{I(r_1, r_2; \theta_1, \theta_2)}{\pi(R_P^2 - R_H^2)\Delta x} \tag{10}$$

where R_P and R_H are the radius of a propeller and a hub, respectively.

$$I(r_1, r_2; \theta_1, \theta_2) = \frac{\int_{r_1}^{r_2}\int_{\theta_1}^{\theta_2}\Phi(r,\theta)r\,d\theta\,dr}{\int_{r_H}^{r_P}\int_0^{2\pi}\Phi(r,\theta)r\,d\theta\,dr} \tag{11}$$

where Φ can be expressed as the pressure (or circulation, thrust, etc.) difference between the pressure and suction sides. The thrust distribution is utilized for the present study.

Similarly, the body-force distribution in a propeller rotative direction can be expressed as in the following equation utilizing torque and distribution function (J):

$$\iiint_V rf_{b\theta}\,dV = Q\iiint_V \frac{I(r_1, r_2; \theta_1, \theta_2)}{\pi(R_P^2 - R_H^2)\Delta x}\,dV \tag{12}$$

$$f_{b\theta} = Q\frac{J(r_1, r_2; \theta_1, \theta_2)}{\pi r(R_P^2 - R_H^2)\Delta x} \tag{13}$$

$$J(r_1, r_2; \theta_1, \theta_2) = \frac{\int_{r_1}^{r_2}\int_{\theta_1}^{\theta_2} \Phi(r,\theta) r^2 \, d\theta \, dr}{\int_{r_H}^{r_P}\int_{0}^{2\pi} \Phi(r,\theta) r^2 \, d\theta \, dr} \tag{14}$$

where Φ is torque distribution.

2.4. Volume fraction equation

The free surface, the boundary surface of the water (p) and the air (q), is acquired from the continuity equation for the volume fraction (α) expressed as

$$\sum_{q=1}^{p}\left[\frac{\partial}{\partial t}(\alpha_q \rho_q) + \nabla \cdot (\alpha_q \rho_q \vec{V})\right] = 0 \tag{15}$$

2.5. Numerical analysis method

To solve the governing equations, the flow domain is subdivided into a finite number of cells and these equations are changed into algebraic form via the discretization process. The cell-centered finite volume method is used for the space discretization. The convective terms are discretized using the QUICK (Quadratic Upwind Interpolation for Convective Kinematics) scheme (Leonard and Mokhtari, 1990). The diffusion terms utilize the central difference scheme. The SIMPLEC (Semi-Implicit Method for Pressure-Linked Equations Consistent) algorithm is applied to the velocity–pressure coupling (Patankar and Spalding, 1972). In the case of the free-surface flow computations, the 1st order backward implicit formulation and the modified HRIC (high-resolution interface capturing) scheme are applied to the VOF and volume fraction discretization, respectively.

3. Computational prediction of speed performance

The speed performance was predicted via analyzing the computational results of the following four cases:

Case 1: Viscous-flow calculation in the towing condition utilizing the free-surface model to obtain total resistance (R_{TM}).
Case 2: Viscous-flow calculation in the towing condition utilizing the double-body model to obtain viscous resistance (R_{VM}).
Case 3: Viscous-flow calculation in the self-propulsion condition utilizing the double-body model to obtain viscous resistance (R_{SP}^{VM}).
Case 4: Unsteady potential-flow calculation to obtain thrust (T_M), torque (Q_M), thrust and torque distribution functions.

In the case of towing computations (Cases 1 and 2), a rudder is not equipped on the hull like the resistance model test; as it is considered to be a propulsor, not an appendage. For self-propulsion conditioned computations (Case 3), an asymmetry body-force propeller and a rudder are equipped on the hull, such as in the self-propulsion model tests. The computations of Cases 3 and 4 are iteratively conducted until the thrust and torque converge at a given propeller rotative speed (n_M).

Fig. 2 presents the process involving the prediction of the speed performance. The model ship is not allowed to move vertically and horizontally. The propeller open-water characteristic curve from the model test was utilized.

3.1. Resistance characteristics

The form factor $(1+k)$ is obtained from

$$1 + k = C_{VM}/C_{FM} \tag{16}$$

where M refers to the model scale and C_{VM} is the viscous resistance coefficient. It is assumed that C_{VM} is the same as the

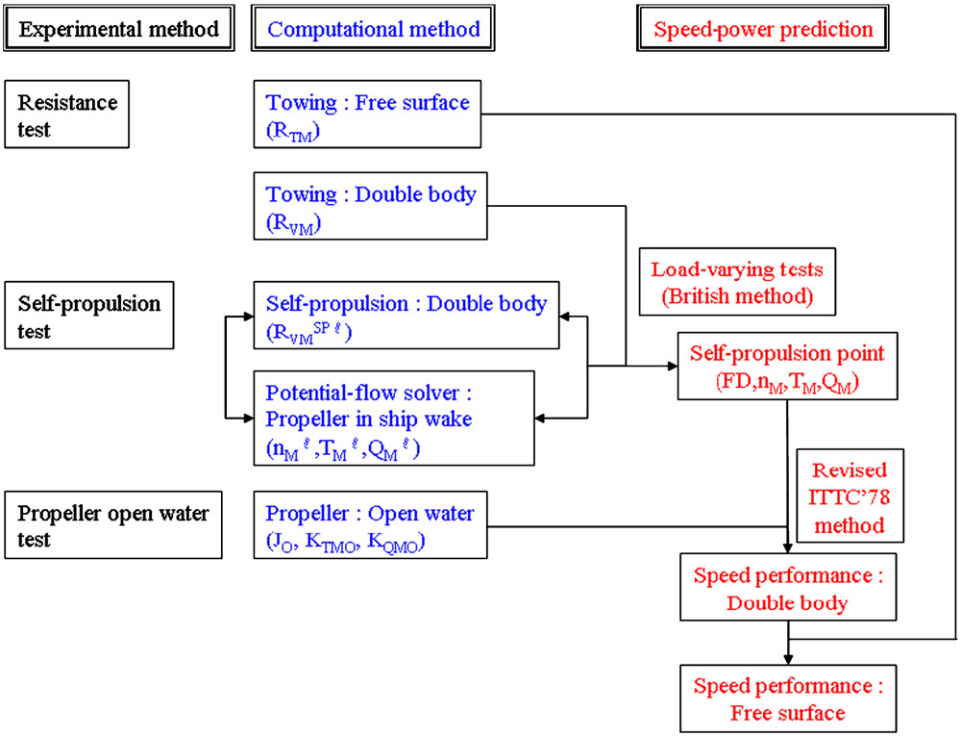

Fig. 2. Procedure to predict the speed performance based on a computational method.

total resistance of the double-body model. C_{FM} [$=0.075/(\log_{10} R_N-2)^2$, $R_N=V_0L/\nu$, where V_0 and L are ship speed and ship length, respectively] is the frictional resistance coefficient obtained from the ITTC-1957 model-ship correlation line. All the resistance coefficients are non-dimensionalized by $0.5\rho SV_0^2$, where S is the wetted surface.

The residual resistance coefficient (C_R) is assumed to be the difference of the total resistance coefficients in the towing computations which apply the free-surface (C_{TM}) and the double-body (C_{VM}) models and is expressed as

$$C_R = C_{TM} - C_{VM} \tag{17}$$

Note that the computational conditions are slightly different from the experimental conditions, i.e., the model ship was restricted in vertical motion and the double-body model was used to treat the free surface, etc. These are the reasons why the correlation coefficient of the CFD-model test is introduced. The CFD-model correlation coefficients of $\Delta C_{FM}-\Delta w_M$ are deduced from the similar concept of the model-ship correlation coefficient $\Delta C_F-\Delta w_C$ (Lindgren et al., 1978). The ΔC_{FM} and Δw_M are coefficients that correct the difference of the total resistance coefficient and propeller rotative speed between the experimental and the computational predictions, respectively.

$$\Delta C_{FM} = \Delta C_F + (C_{TM}^E - C_{TM}^C) \tag{18}$$

$$\Delta C_F = [105(k_S/L_{WL})^{1/3} - 0.64] \times 10^{-3} \tag{19}$$

where the superscript E and C indicate the experiment and the calculation, respectively. k_S ($=150\times10^{-6}$ m) is the hull roughness in a real ship scale. Δw_M is to be discussed later. Then the total resistance coefficient of the ship (C_{TS}) is written as

$$C_{TS} = \frac{S_S + S_{BK}}{S_S}[(1+k)C_{FS} + \Delta C_{FM}] + C_R + C_{AA} \tag{20}$$

$$C_{AA} = 0.001\frac{A_T}{S_S} \tag{21}$$

where BK denotes the bilge keel. C_{AA} and A_T denote the air resistance coefficient and the projected area of a superstructure, respectively. It is assumed that the scale effect of the form factor is negligible.

The effective power (P_E) is expressed as

$$P_E = C_{TS}\frac{1}{2}\rho_S S_S V_S^3 \tag{22}$$

3.2. Self-propulsion point

In the self-propulsion computations for the given V_M and n_M, the iterative processes between the viscous- and the potential-flow calculations are performed until T_M and Q_M converge as mentioned above. Three or four iterations are enough to get the converged solutions as shown in Fig. 3.

In order to predict speed performance, it is necessary to obtain a self-propulsion point of a ship. The self-propulsion point may be found in the results of the towing and the self-propulsion computations under- and over-loaded propeller conditions for the given V_M. In model scale, the difference in force between the viscous ship resistance and the propeller thrust [the so-called

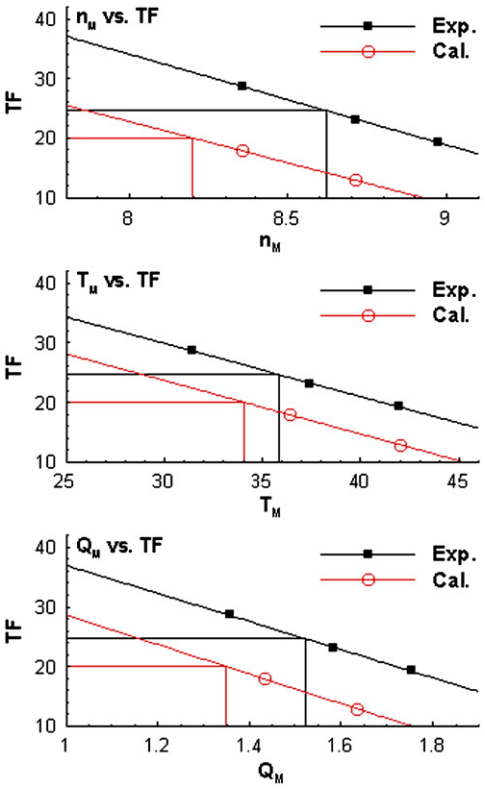

Fig. 4. Procedure to obtain a self-propulsion point: 5600 TEU container carrier.

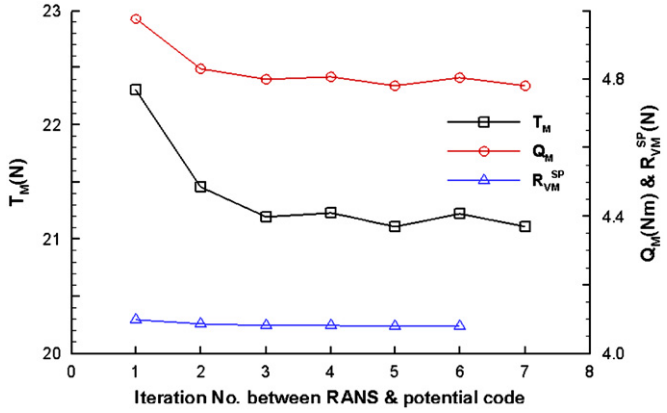

Fig. 3. Convergence history of self-propulsion computations: 319K VLCC, n_M=8.00 rps.

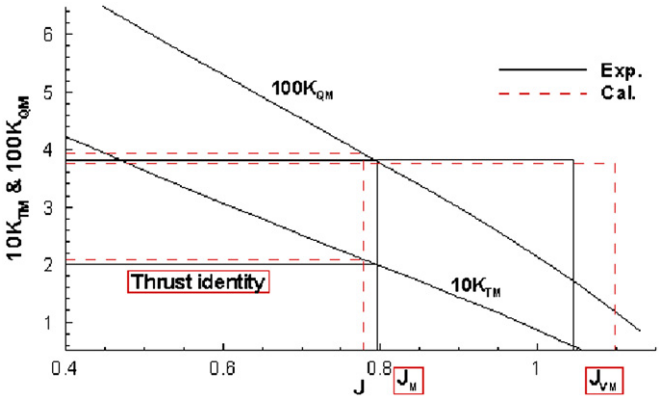

Fig. 5. Method to obtain wake fraction and rotative efficiency—thrust identity: 5.600 TEU container carrier.

'towing force (TF)'] is zero at the self-propulsion point

$$TF = R_{VM}^{SP} - T_M \tag{23}$$

In a full ship scale, however, the value of TF should be corrected by the viscous force difference between the model and the ship scale (Lindgren et al., 1978; Choi et al., 2009) as shown below

$$FD = 1/2\rho_M S_M V_M^2 (C_{VM} - C_{VS}) = 1/2\rho_M S_M V_M^2 [(1+k)(C_{FM} - C_{FS}) - \Delta C_{FM}] \tag{24}$$

$$C_{VS} = (1+k)C_{FS} + \Delta C_{FM} \tag{25}$$

The values of n_M, T_M, and Q_M at the self-propulsion point are obtained from interpolating those self-propulsive computational results at the value of FD. Fig. 4 presents the procedure to obtain n_M, T_M and Q_M at FD of the self-propulsion point.

3.3. Self-propulsion characteristics

The self-propulsion factors are obtained using the revised ITTC'78 method.

Thrust deduction fraction (t) is obtained from

$$t = \frac{R_{VM}^{SP} - R_{VM}}{T_M} \tag{26}$$

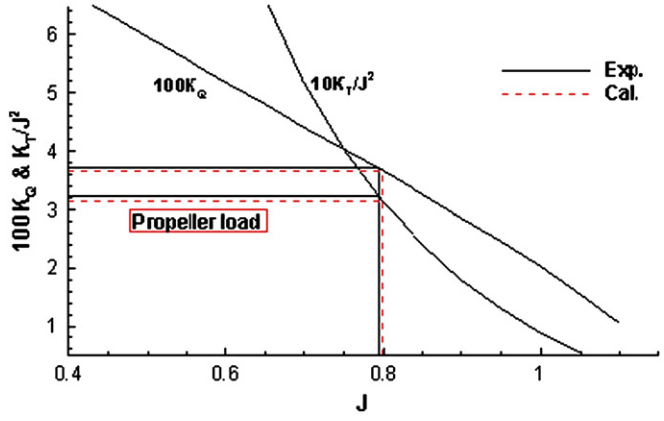

Fig. 6. Method to find the operating point of the ship propeller: 5.600 TEU container carrier.

Wake fraction (w) and relative rotative efficiency (η_R) are obtained through utilizing the propeller-open-water curves based on a 'thrust-identity method' as shown in Fig. 5:

$$w_M = 1 - \frac{J_M}{J_{VM}} + \Delta w_M \tag{27}$$

$$\eta_{RM} = \frac{Q_{OM}}{Q_M} \tag{28}$$

where J is the advance ratio of the propeller. The subscript O denotes the open-water condition. As discussed earlier, Δw_M is the CFD-model test correlation coefficient to correct the propeller rotative speed and may be expressed as

$$\Delta w_M = \frac{J^C}{J^E}(1 - w_M^E) - (1 - w_M^C) \tag{29}$$

It is assumed that t and η_R have no scale effects. w_S and hull efficiency (η_H) are obtained, respectively, from the following equations:

$$w_S = (t + 0.04) + (w_M - t - 0.04)\frac{C_{FS}}{C_{FM}} \tag{30}$$

$$\eta_H = \frac{1-t}{1-w_S} \tag{31}$$

From the intersection of the propeller load (K_T/J^2) and the propeller open-water curves in full scale as shown in Fig. 6, n_S, delivered power (P_{DS}^{DB}), and propulsive efficiency (η_D^{DB}) at the operating point may be obtained

$$\frac{K_{TS}}{J_{OS}^2} = \frac{S_S}{2D_S^2}\frac{C_{VS}}{(1-t)(1-w_S)} \tag{32}$$

$$n_S = \frac{(1-w_S)V_S}{J_{OS}D_S} \tag{33}$$

$$P_{DS}^{DB} = 2\pi n_S^3 D_S^5 K_{QOS}/\eta_R \tag{34}$$

$$P_E^{DB} = C_{VS}\frac{1}{2}\rho_S S_S V_S^3 \tag{35}$$

$$\eta_D^{DB} = \frac{P_E^{DB}}{P_{DS}^{DB}} \tag{36}$$

where D is the diameter of a propeller. Superscript DB denotes the double-body model. Note that all the above results do not take the free surface into consideration.

Table 1
Principal particulars for the objective ships and propellers.

Ship name	5600 CC	6800 CC	7200 CC	7800 CC	319K VLCC	172K BC	150K LNGC	216K LNGC
L_{PP} (m)	271.00	286.00	304.00	319.93	319.00	279.00	275.00	303.00
B (m)	40.00	42.80	42.80	42.80	60.00	45.00	44.20	50.00
T (m)	12.50	13.50	13.00	13.00	21.60	16.50	11.35	12.00
C_B [L_{WL}]	0.5912	0.6509	0.6592	0.6488	0.7983	0.8289	0.7582	0.7623
S (m^2)	12,780	15,174	15,876	16,545	28,509	19,123	14,743	18,840
A_T (m^2)	1120	1465	1444	1600	1182	699	1300	14,940
S_{BK} (m^2)	96.0	135.9	150.0	160.0	160.0	108.8	165.0	181.8
F_N [L_{WL}]	0.250	0.237	0.241	0.235	0.141	0.146	0.195	0.184
λ[a]	41.513	40.445	42.063	42.063	47.085	39.605	35.833	40.000
$R_N \times 10^6$ [L_{WL}]	9.77	11.74	12.08	11.43	6.99	6.81	10.43	9.00
Z[b]	5	6	6	6	4	4	4	4
R_P (m)	4.60	4.375	4.60	4.60	4.95	4.05	4.30	3.80
R_H (m)	0.808	0.830	0.980	0.980	0.680	0.640	0.763	0.815

[a] Scale ratio.
[b] Number of blade.

Table 2
Comparison of hull-form characteristics for the objective ships.

	5600 CC	6800 CC	7200 CC	7800 CC	319K VLCC	172K BC	150K LNGC	216K LNGC
Bulbous bow	H[a]	H	H	H	M[b]	L[c]	H	H
Stern shape	V[d]	V	V	V	U[e]	U	U	T[f]
Transom	D[g]	D	D	D	W[h]	W	D	D
Design waterline at stem	C[i]	C	C	C	E[j]	E	C	C

[a] High nose.
[b] Middle bulb of plank type.
[c] Low nose.
[d] Moderate V-form with stern bulb.
[e] Moderate U-form with stern bulb.
[f] Twin-skeg.
[g] Dry.
[h] Wetted.
[i] Concave type with an inflection point.
[j] Elliptic type with a round ending.

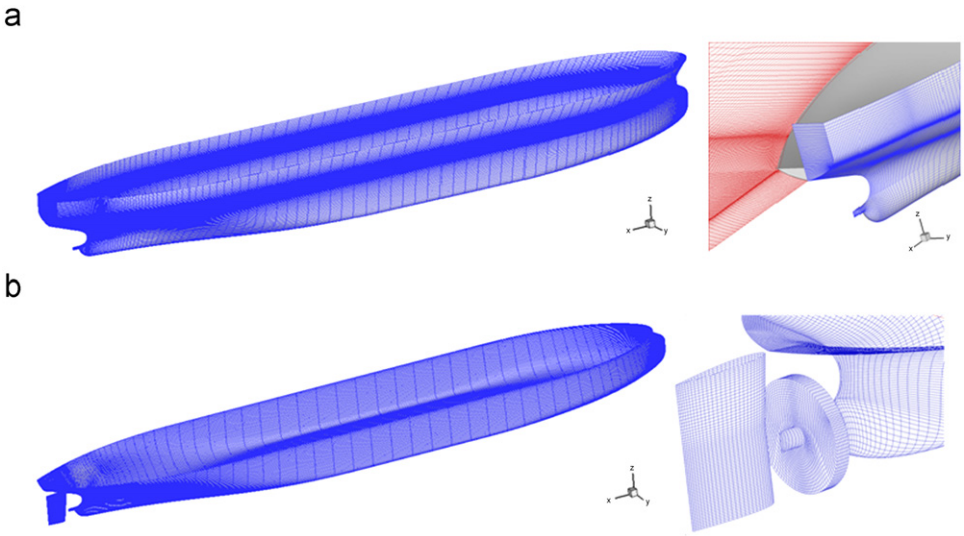

Fig. 7. Over and partial views of grid generation around a ship (319K VLCC): (a) towing condition using free-surface model and (b) self-propulsion condition using double-body model.

Table 3
Number of cells and calculation domain.

	No. of skegs	No. of cells	Calculation domain
Towing (double body)	Single	1,215,000	$-1.00 < x/L_{pp} < 1.50$, $0.00 < y/L_{pp} < 1.00$
	Twin	2,189,640	$-1.00 < z/L_{pp} < 0.00$
Self-propulsion (double body)	Single	2,550,000	$-1.00 < x/L_{pp} < 1.50$, $-1.00 < y/L_{pp} < 1.00$
	Twin	3,605,736	$-1.00 < z/L_{pp} < 0.00$
Towing (free surface)	Single	6,285,000	$-1.00 < x/L_{pp} < 2.00$, $0.00 < y/L_{pp} < 1.00$
	Twin	9,791,487	$-1.00 < z/L_{pp} < 0.03$

Table 4
Grid systems for the uncertainty analysis.

Grid systems	Grid dimensions	No. of cells	y_N^+
GS1	$344 \times 120 \times 86$	3,501,575	60
GS2	$242 \times 61 \times 85$	1,225,440	84
GS3	$168 \times 43 \times 59$	413,070	131

3.4. Speed performances

The delivered power (P_{DS}^{FS}) which takes free surface into consideration may be obtained using the following equation by assuming propulsive efficiency of the double-body model is the same as that obtained from the free-surface model:

$$P_{DS}^{FS} = \frac{P_E^{FS}}{\eta_D^{DB}} \tag{37}$$

4. Selection of objective ships

The objective ships are four large-size container carriers (5600/6800/7200/7800 TEU C/C, hereafter 5600/6800/7200/7800 CC), a

bulk carrier (172,000 TDW B/C, hereafter 172K BC), a VLCC (319,000 TDW VLCC, hereafter 319K VLCC), and two LNG carriers (150,000/216,000 m^3 LNG/C, hereafter 150K/216K LNGC). These eight ships have representative hull forms of the fine high-speed ship (FiHS), the full slow-speed ship (FuSS), and the full medium-speed ship (FuMS), respectively.

Table 1 shows the principal particulars of the objective ships and propellers. Table 2 describes the hull-form characteristics. For the FiHS and FuMS, a higher nose is adopted to get positive effect within a limited range of draught, i.e., design draft. For the FuSS, a lower nose is employed for the 172K BC to get positive effect on the ballast draft. 319K VLCC installed a middle bulb plank type to minimize the shift in ship performance with the change of draft and to generate hull-form with moderate curvature. Transom stern is adopted to ensure cargo space and to secure the advantage in construction. The design waterline shape of the FuSS is elliptic with a round ending, whereas those of the FiHS and FuMS are concave with an inflection point and a sharp ending. The shape of the frame lines at the stern of FiHS is a moderate V-form, whereas those of the FuSS and FuMS are a moderate U-form. All of the objective ships have stern bulbs. The 216K LNGC has a twin-skeg hull form.

Table 5
Verification of viscous resistance coefficient ($C_{VM} \times 10^3$, $\varepsilon \times 10^6$).

S_{Exp}	S_{GS1}	S_{GS2}	S_{GS3}	ε_{G21}	ε_{G32}	R_G	p_G	C_G
3.998	4.015	4.018	4.025	2.744	7.188	0.382	2.779	1.620

Table 6
Error and uncertainties for viscous resistance coefficient.

Uncorrected C_{VM}	Corrected C_{VM}		
U_G	δ_G	U_{GC}	$C_{VM} \times 10^3$
0.402%	0.068%	0.087%	4.012

Table 7
Validation of uncorrected and corrected viscous resistance coefficient.

	E (%)	U_V (%)	U_I (%)	U_{SN} (%)
Uncorrected C_{VM}	−0.424	2.557	0.250	0.476
Corrected C_{VM}	−0.356	2.527	0.250	0.266

5. Grid generation, calculation conditions and uncertainty assessment

5.1. Grid generation

Fig. 7 presents the views of grid generation around a ship at the towing conditions using the double-body and the free-surface models, and the self-propulsion condition using the double-body model. In the towing computations, the rudder is not attached on the model ship; as it is considered as not an appendage but a propulsor. In the self-propulsion computations, an asymmetry body-force propeller and a rudder are equipped on the hull as in the model test. The grid system is the hexahedron grids of O–H type in a multi-block. The propeller disk block is a cylinder with the same axial length and the radius of the propeller at the self-propulsion condition. The grids around the rudder were also generated using body-fitted structured grids. The number of cells for the propeller disk block is 17,600 with 20, 88 and 10 in the radial, tangential and axial direction, respectively.

Table 8
Verification of wall shear resistance coefficient ($C_\tau \times 10^3$,$\varepsilon \times 10^5$).

$C_{\tau\ GS1}$	$C_{\tau\ GS2}$	$C_{\tau\ GS3}$	ε_{21}	ε_{21}	R_G	p_G	C_G
3.198	3.210	3.250	1.139	3.981	0.286	3.610	2.494

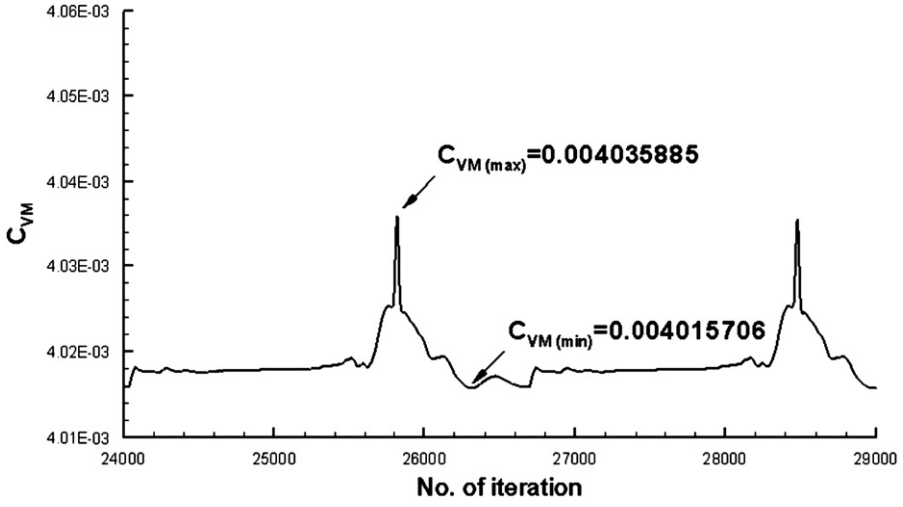

Fig. 8. Iterative history of C_{VM} in GS2.

The number of cells and calculation domain are shown in Table 3.

5.2. Calculation conditions

The calculations are carried out at the design speed in a model scale. In the computations using the double-body model, velocity inlet, symmetry, and outflow conditions are applied for the inlet, the side/top/bottom, and the outlet boundary plane, respectively. The computations using free-surface model apply pressure inlet, pressure outlet, and symmetry conditions for the inlet, the outlet, and center/side/top/bottom boundary planes, respectively. The standard wall function is used to enhance computational efficiency.

5.3. Uncertainty analysis

The uncertainty analysis is carried out utilizing the computational results of three grid systems (GS1, GS2, GS3) at the towing condition applying the double-body model of a 319K VLCC, as shown in Table 4, where y_N^+ is the 1st grid space from the hull in the wall coordinate, which are in the log-law region. GS1, GS2 and GS3 are the fine, medium and coarse grid systems, respectively, with constant refinement ratio ($r_G = \Delta x_2/\Delta x_1 = \Delta x_3/\Delta x_2 = \sqrt{2}$). GS2 is a reference grid system because it is used in the main subject, where the speed performances are predicted by analyzing the resistant and propulsive characteristics of the objective ships. While the percentage errors and uncertainties are relative values with respect to C_{VM} of GS2 in verification procedures, the percentage values are based on the experimental result in

Table 9
Fullness parameters of various types of commercial ships.

Ship name	5600 CC	6800 CC	7200 CC	7800 CC	319K VLCC	172K BC	150K LNGC	216K LNGC
a=1.3 and b=3.1	0.321	0.379	0.356	0.329	0.512	0.494	0.533	0.569
a=1.1 and b=0.8	0.343	0.404	0.390	0.361	0.745	0.742	0.618	0.643

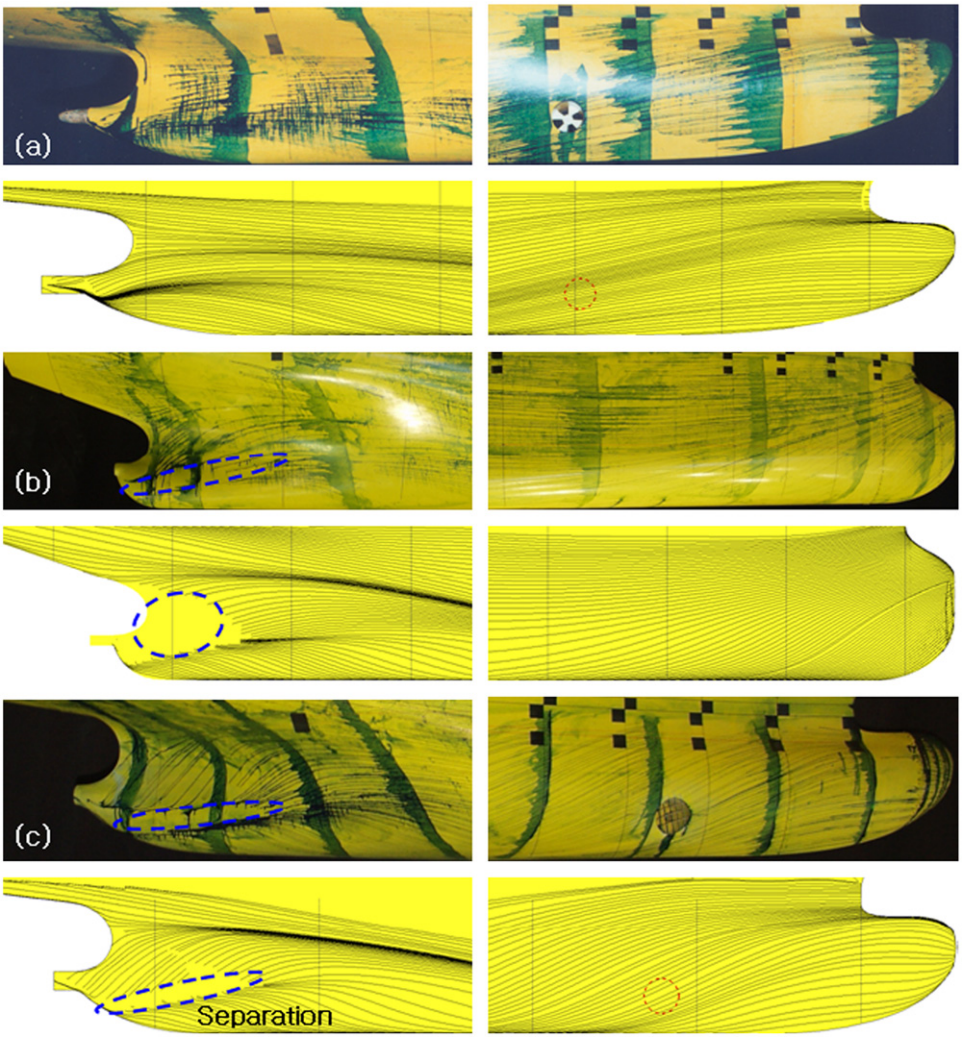

Fig. 9. Limiting streamlines on the hull (a) 5600 CC; (b) 319K VLCC and (c) 150K LNGC.

validation procedures. The hexahedron cell shape is applied. The grids are composed of multi-block with an O–H type. The calculation domains are $-1.0 < x/L_{PP} < 1.5$, $0.0 < y/L_{PP} < 1.5$ and $-1.0 < z/L_{PP} < 0.0$.

The computational results of C_{VM} are verified for the grid systems as shown in Table 5, where S_{Exp} and S_{GSi} are the experimental and the computational values of i-grid systems, respectively. Convergence ratio (R_G), order of accuracy (p_G) and correction factor (C_G) are defined as follows:

$$R_G = \varepsilon_{G21}/\varepsilon_{G32} \tag{38}$$

$$\varepsilon_{Gij} = S_{GSi} - S_{GSj} \tag{39}$$

$$p_G = \frac{\ln(\varepsilon_{G32}/\varepsilon_{G21})}{\ln r_G} \tag{40}$$

$$C_G = \frac{r_G^{p_G} - 1}{r_G^{p_{Gest}} - 1} \tag{41}$$

where p_{Gest} is the estimate for the limiting order of accuracy. Since $0 < R_G < 1$, the monotonic convergence of C_{VM} may be assumed. This means that the generalized Richardson extrapolation (RE) may be used to estimate both errors and uncertainties. As reported in Xing and Stern (2008), the modified correction factor by Wilson et al. (2004) gives a valid estimation of uncertainties for $C_G < 1$ because the factor of safety is too small for $C_G > 1$. Since C_G is larger than 1 in the present study, the improved uncertainty estimates of Xing and Stern (2008) are used to obtain more reasonable intervals of uncertainty for $C_G > 1$. The

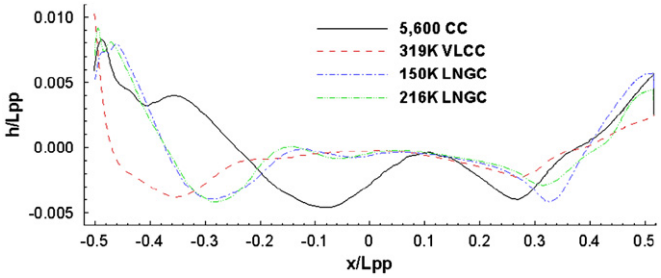

Fig. 11. Wave profiles on the hull.

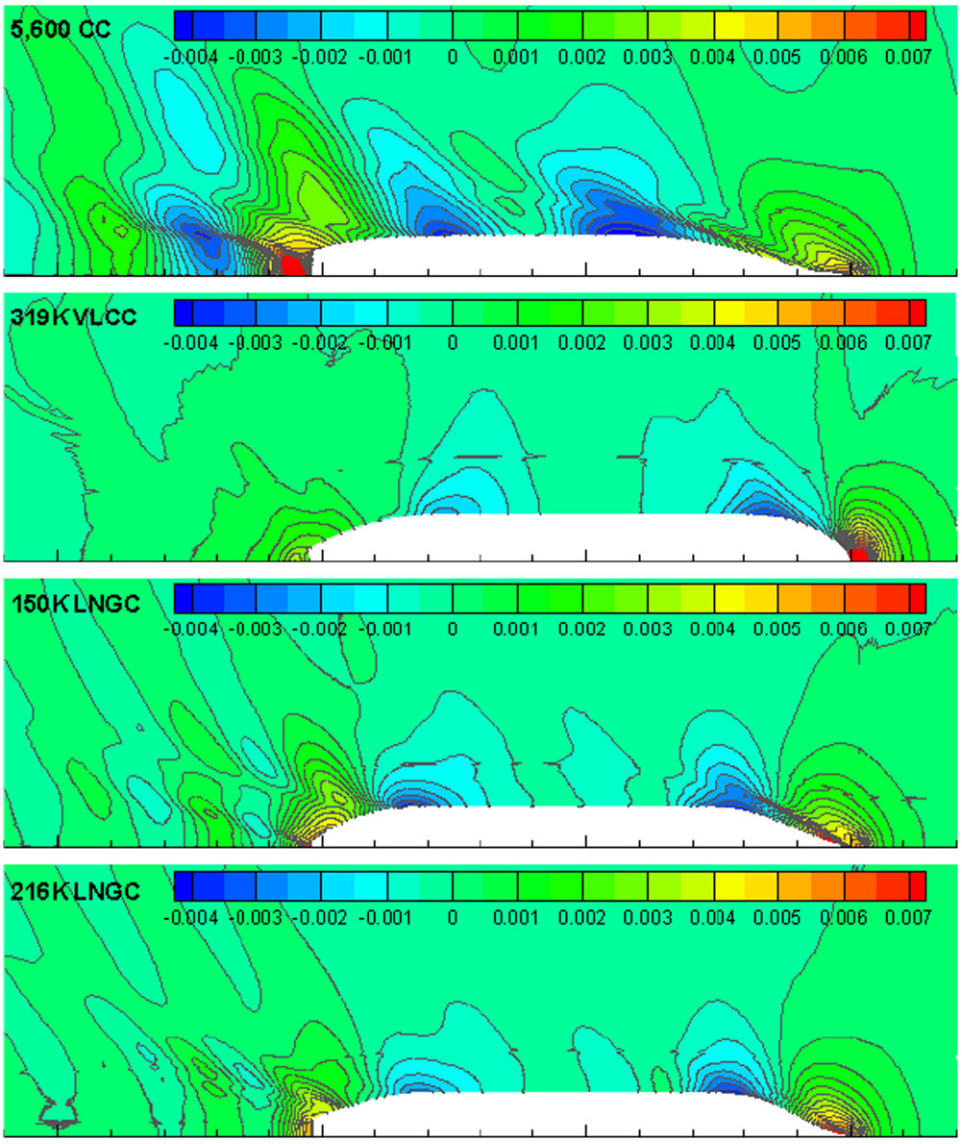

Fig. 10. Comparison of wave patterns around various types of model ships.

error and the uncertainties of the computational values of C_{VM} are shown in Table 6, where numerical uncertainty (U_G), numerical error (δ_G), numerical uncertainty of corrected value (U_{GC}) are defined as follows:

$$U_G = \frac{C_G}{2-C_G}[2(C_G-1)+1]|\delta_G| \quad \text{for } 1.125 \le C_G \le 2 \tag{42}$$

$$U_{GC} = \frac{C_G^2+2C_G-3}{3-C_G}|\delta_G| \quad \text{for } 1.25 \le C_G \le 2 \tag{43}$$

$$\delta_G = C_G \frac{\varepsilon_{G21}}{r_G^{p_G}-1} \tag{44}$$

$$C_{VMC} = C_{VM} - \delta_G \tag{45}$$

The error can be estimated as -0.170×10^{-4} corresponding to 0.424% of C_{VMExp}. When C_{VM} is undercompensated with the error, C_{VM} is calculated 4.012×10^{-3} as which represents the limiting value when the asymptotic range is reached.

The results of the validation for C_{VM} are listed in Table 7, where comparison error (E), validation uncertainty (U_V) and numerical uncertainty (U_{SN}) are defined as follows:

$$E = S_{Exp} - S_{GS1} \tag{46}$$

$$U_V^2 = U_D^2 + U_{SN}^2 \tag{47}$$

$$U_{SN}^2 = U_G^2 + U_I^2 + U_T^2 \tag{48}$$

Here the iterative uncertainties (U_I) of GS2 are quantified by examining the fluctuations of C_{VM} in the last a few periods of convergent history. Fig. 8 shows a portion of the iterative history in which the fluctuations is about 0.50% of C_{VM} over the last two periods of variations. The iterative uncertainties (U_I) are estimated as a half of the C_{VM} fluctuations, i.e., U_I=0.25%. Numerical uncertainty due to time step (U_T) is zero in the present problem. When the experimental uncertainty (U_D) is generally assumed to be 2.5%, the validation of the present numerical simulations is achieved because both errors of uncorrected and corrected C_{VM} are much smaller than U_V. Consequently the numerical value of 4.018×10^{-3} is valid for estimating the viscous resistance of the model ship.

In principle, making precise estimations requires the grid sizes near and far from the wall to be scaled either up or down with the same ratio of grid refinement as reported in the 23rd ITTC (2002). If y^+ is smaller than 1, the contribution of modeling errors to C_{VM} may be completely excluded without adopting any wall function. In engineering applications, however, it is inevitable to use a wall function for numerical efficiency by assuming that the function provides consistent distributions of wall shear stress on the hull, as long as y^+ is in the log-law region. Now the key issue is whether a consistency of wall shear resistance coefficient (C_τ) may be obtained from the standard wall function used in the present study when y^+ varies from 60 to 131. The results are briefly summarized in Table 8. As shown in Table 8, the convergence ratio is in the range of $0<R_G<1$. This means that the grid convergence of the wall shear resistance is verified even if the standard wall function is used in the present study.

6. Results and discussions

The speed performances are closely related to the fullness of hull form. Sasajima and Tanaka (1974) proposed the fullness parameter (γ_A) as expressed below

$$\gamma_A = \frac{B/L}{a(1-C_B)+bL_{CB}/L} \tag{49}$$

where a and b are the constants. Sasajima and Tanaka (1974) employed a=1.3 and b=3.1. This study uses a=1.1 and b=0.8 in order to clearly exhibit the fullness of the FuMS. The values of γ_A are listed in Table 9.

6.1. Limiting streamlines on the hull

Fig. 9 compares the limiting streamlines on the stern hull from the calculations with those of model tests. The streamlines on the hull offer valuable design information regarding the grid angle of a bow thruster, the location to attach the bilge keel or appendages such as energy saving devices, and the wake characteristics of the propeller plane. The circular dotted line in 5600 TEU CC and 150K LNGC calculations indicate the bow thruster. An interesting fact is that the flow is separated at the stern in the case of moderate U-form as displayed in blue dotted lines (319K VLCC and 150K LNGC). This flow separation is why the incoming velocity decreases on the propeller plane. The limiting streamline on the hull is also useful to understand the axial-vorticity distribution on the propeller plane since it is a footprint of vortices.

6.2. Wave characteristics around a ship

Fig. 10 compares the characteristics of wave patterns around the ships. The wave elevation is non-dimensionalized by L_{PP}. These characteristics differ greatly according to the types of ships. This is thought to be due to the differences in shapes of the bulbous bows and waterlines as described in Table 2. The divergent wave is clear near FiHS and FuMS, and not as much with FuSS.

Fig. 11 compares the wave profiles on the hulls. The stem wave profile of the FuSS is far greater compared to those of other ship

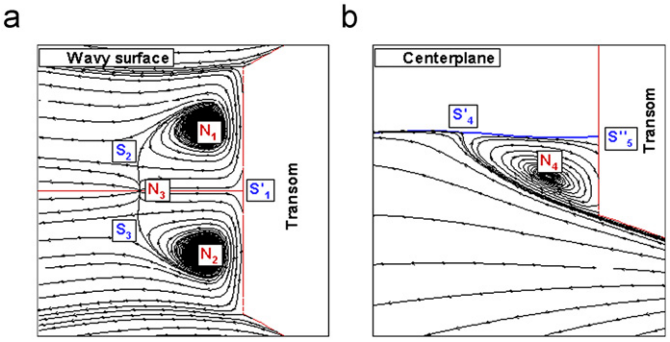

Fig. 12. Streamline pattern on wavy surface and centerplane behind transom of 319K VLCC.

Table 10
Theoretical Kelvin wave length and bow wave length of commercial ships.

Ship name	5600 CC	6800 CC	7200 CC	7800 CC	319K VLCC	172K BC	150K LNGC	216K LNGC
$2\pi F_N^2$	0.393	0.353	0.365	0.347	0.125	0.134	0.239	0.213
λ/L	0.420	0.323	0.322	0.328	0.151	0.093	0.207	0.212

types. In the case of the twin-skeg ship (216K LNGC), compared to a single-skeg ship (150K LNGC), the stem wave profile is similar but it is lower at the stern. The bow wave length (λ/L), where it is assumed to be the length from FP to the 1st wave trough on the wave profile on the hull, is closely proportional to the theoretical Kelvin wave lengths ($2\pi F_N^2$) as listed in Table 10.

The free-surface flow around the transom stern is complicated, due to suddern changes of hull curvature resulting from the wetted transom. Fig. 12 presents streamline pattern on the wavy surface and the centerplane behind transom of a 319K VLCC. On the wavy surface, there are two symmetrical vortical flows with spiral nodes in port (N_1) and starboard (N_2) sides at (0.530, $\pm$0.128, ζ) due to flow separation, where ζ is wave elevation. Along the centerline on the wavy surface, one node (N_3) exists at (0.543, 0.000, ζ) and the reverse flow from this node meets at transom with a half-saddle point (S_1'). The flow from this node (N_3) combines with those from the spiral node N_1 (or N_2) and separates at a saddle point S_2 (or S_3) located at (0.544, $\pm$0.005, ζ). The topological rule (Tobak and Peake, 1982) is expressed as follows:

$$\sum N - \sum S = 3 - 2\frac{1}{2} = \frac{1}{2} \tag{50}$$

On the centerplane, a vortical flow exists with a spiral node (N_4) at (0.530, 0.000, -0.003). The flow from this spiral node N_4 combines at a half-saddle point (S_4') on the wavy surface at (0.543, 0.000, ζ), which is the same location of N_3. The reverse flow from this node (S_4') meets at transom with a quarter-saddle point (S_5''). The topological rule is expressed as follows:

$$\sum N - \sum S = 1 - \frac{3}{4} = \frac{1}{4} \tag{51}$$

This flow behind the transom stern has the same structure of the flow obtained from the experiments (Yamano et al., 2000). There is reverse flow at the stern end ($N_3 \rightarrow S_1'$ or $S_4' \rightarrow S_5''$), the reverse flow stops once near the stern end (S_1' or S_5''), moves along the stern end to each of the sides, and flows out along the sides. A part of the reverse flow gets mixed with the under-flow.

Fig. 13 presents the contours of wave elevation and axial velocity on transom wavy surface. The velocity is non-dimensionalized by the design speed (V_0). Even in the fixed model condition with dry transon in rest (such as 5600 CC, 150K LNGC and 216K LNGC), the transom is submerged in sailing due to the upward wave along the stern. This transom immersion leads to resistace increase due to pressure loss.

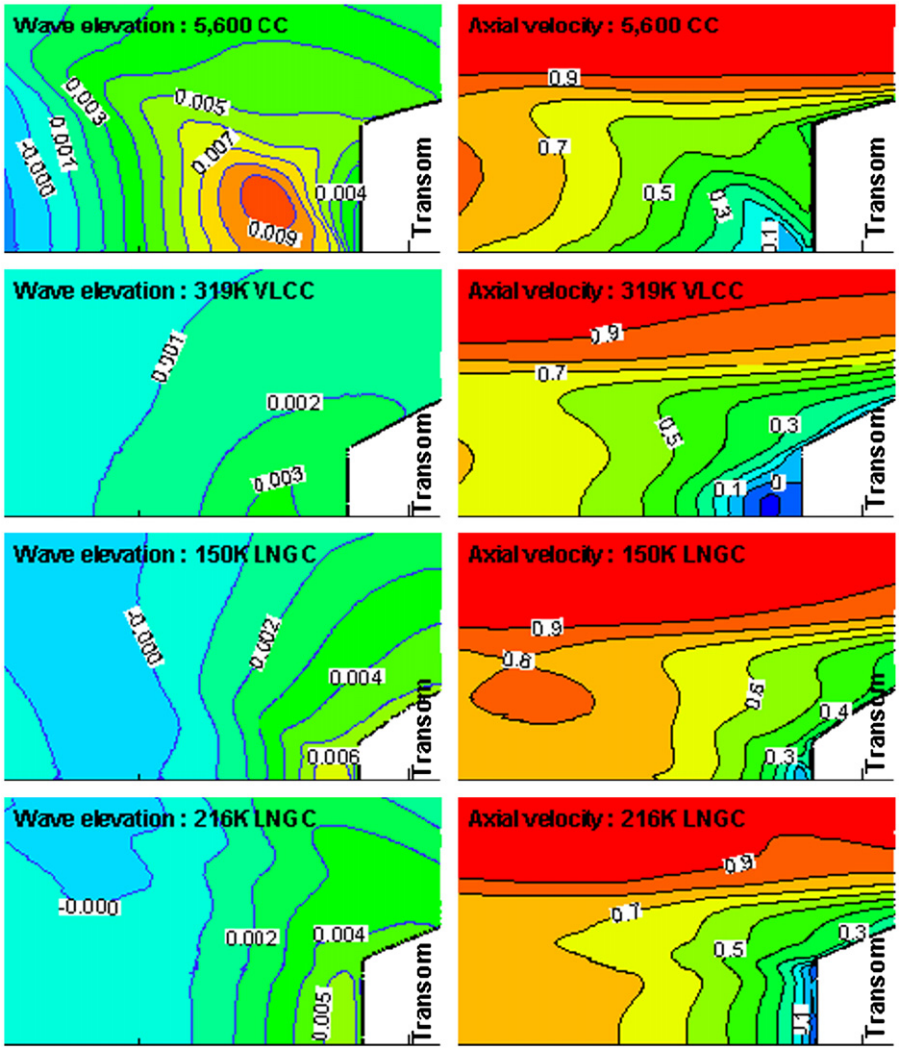

Fig. 13. Contours of wave elevation and axial velocity on transom wavy surface of various types of ships.

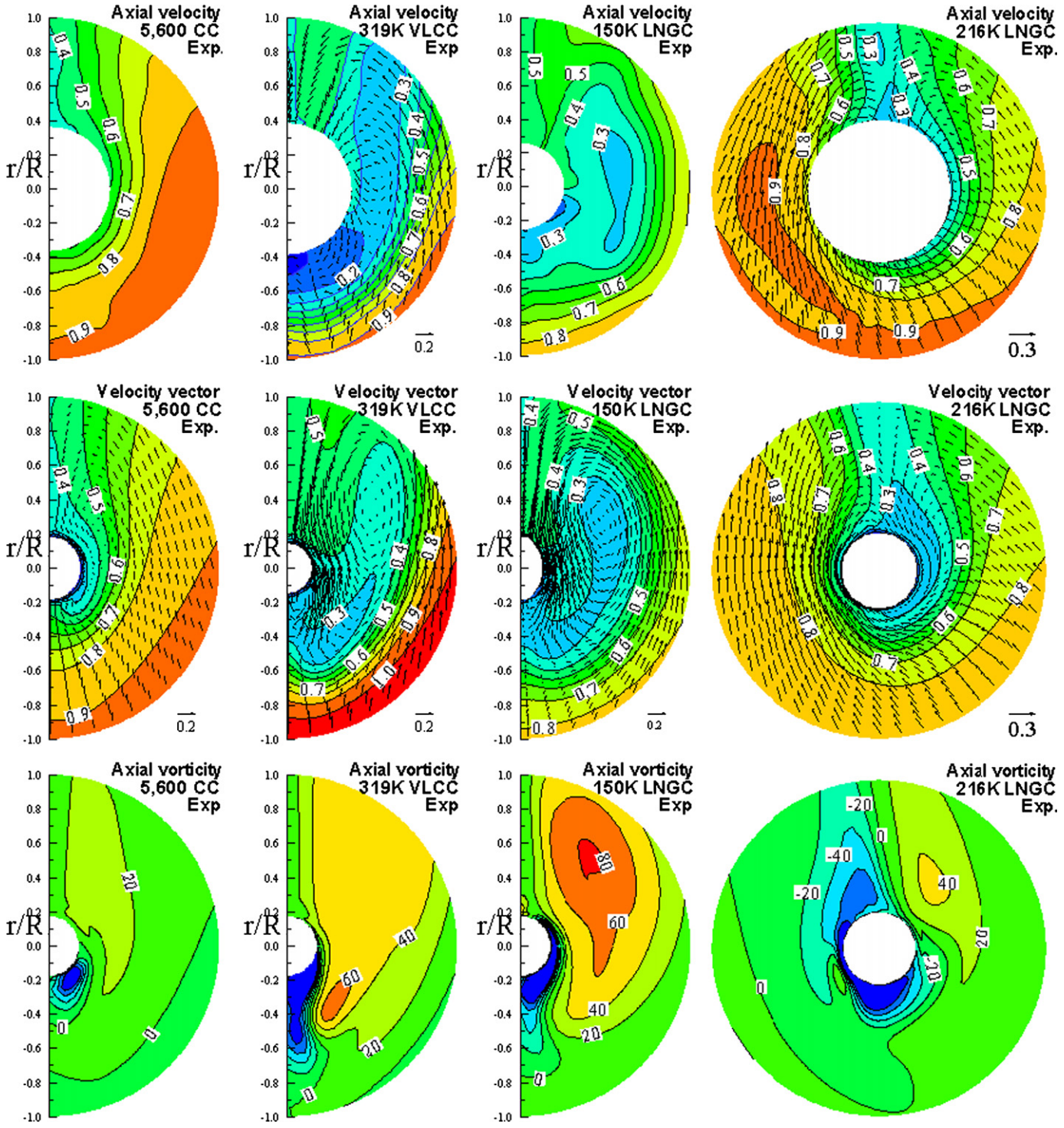

Fig. 14. Contours of axial velocity, velocity vector and axial vorticity on the propeller plane.

6.3. *Wake characteristics on the propeller plane*

Fig. 14 presents the axial velocity contour, velocity vector and axial-vorticity contour on the propeller plane. The vorticity is non-dimensionalized by V_0 and L_{PP}. The wake characteristics on the propeller plane in the towing condition offer critical information in designing propellers. One of the wake characteristics on the propeller plane in the case of FuMS and FuSS is the low-speed peak in the shape of an island (the so-called 'hook shape') and is well displayed in the results of the model test and calculations. This 'hook shape' is deemed to be the impact of the bilge vortices which develop around the stern and can also be predicted from the limiting streamlines in Fig. 9. These bilge vortices are the causes of large secondary flow. In the case of FiHS, there is no 'hook shape', but a slight secondary flow is observed. In the case of FuSS, a low-speed area exists in the lower part of the

propeller axis which puts great load on the propeller. Twin-skeg ship displays greater axial velocity and secondary flows in the inner part of the skegs. The magnitude of the axial vorticity is dependent on that of the secondary flow.

Fig. 15 presents the radial distribution of the circumferentially average axial velocity ($\overline{V}_x$) on the propeller plane. The values of $\overline{V}_x$ on the propeller plane differ greatly between FiHS and FuMS/FuSS. The regions with large speed slopes include 0.3–0.55r/R in FiHS and 0.55–0.9r/R in FuMS/FuSS. In terms of twin-skeg ship, even if it is a FuMS, it shows similar shape of FiHS.

6.4. Resistance characteristics

The resistance characteristics for the various types of ships are summarized in Table 11.

Fig. 16 presents the relationship between form factor and γ_A. The dotted line denotes tendency line of the computational predictions. The form factor increases as the hull form becomes fuller. In the case of FiHS and FuMS, the computational predictions are 5.7% lower compared to the experimental ones, whereas the experimental and the computational predictions are nearly same in the case of FuSS. In the cases of FiHS and FuMS, the fact that the experimental predictions are larger than the computational predictions is deemed to be due to the

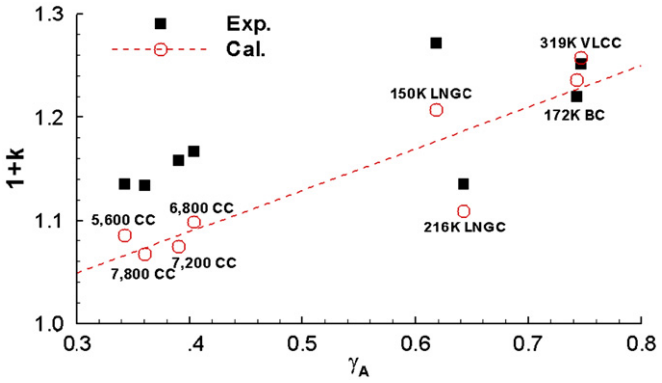

Fig. 16. Relationship between form factor and fullness parameter.

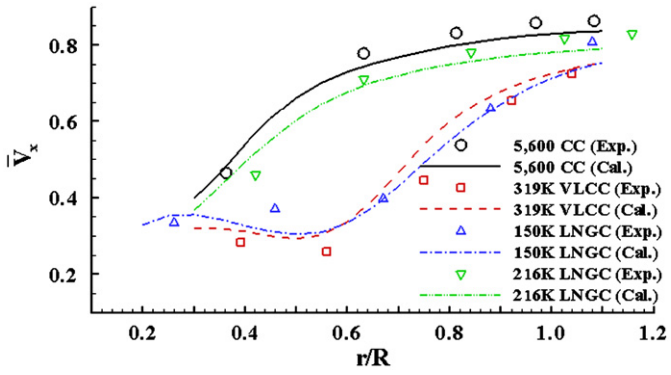

Fig. 15. Circumferentially averaged axial velocity on the propeller plane.

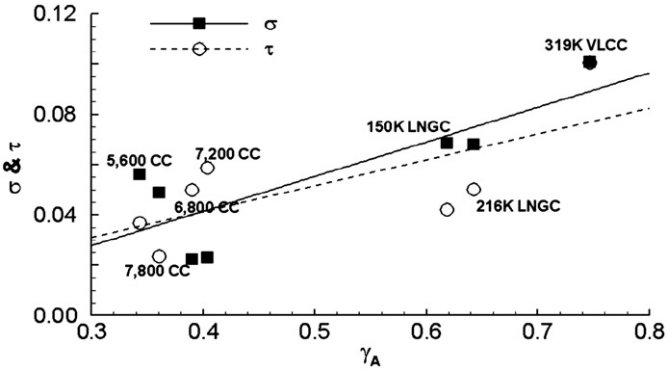

Fig. 17. Sinkage and trim coefficient of various types of ships.

Table 11
Summary of resistance characteristics for the various types of ships.

		5600 CC	6800 CC	7200 CC	7800 CC	319K VLCC	172K BC	150K LNGC	216K LNGC
$1+k$	Cal.	1.085	1.098	1.074	1.067	1.257	1.236	1.207	1.109
	Exp.	1.135	1.167	1.158	1.134	1.251	1.220	1.271	1.135
	Diff. (%)	−4.41	−5.91	−7.25	−5.91	0.48	1.31	−5.04	−2.29
$C_{TM} \times 10^3$	Cal.	3.437	3.322	3.332	3.266	4.076	3.878	3.529	3.386
	Exp.	3.669	3.611	3.595	3.506	4.057	3.975	3.850	3.571
	Diff. (%)	−6.32	−8.00	−7.32	−6.85	0.47	−2.44	−8.34	−5.18
$C_R \times 10^3$	Cal.	0.168	0.117	0.213	0.138	0.058	−0.091	−0.067	−0.003
	Exp.	0.251	0.205	0.233	0.182	0.060	0.058	0.065	0.103
	Diff. (%)	−33.07	−42.93	−8.58	−24.18	−3.33	−256.9	−203.1	−102.9
C_R/C_{TM} (%)	Cal.	4.89	3.52	6.39	4.23	1.42	−2.35	−1.90	−0.09
	Exp.	6.84	5.68	6.48	5.19	1.48	1.46	1.69	2.88
$\Delta C_{FM} \times 10^3$	Cal.	0.455	0.494	0.455	0.418	0.152	0.306	0.543	0.375
	Exp.	0.223	0.205	0.192	0.178	0.171	0.209	0.222	0.190
$C_{VS} \times 10^3$	Cal.	1.916	1.964	1.879	1.824	1.902	2.062	2.215	1.891
	Exp.	1.750	1.767	1.726	1.673	1.912	1.942	1.982	1.741
	Diff. (%)	9.49	11.15	8.86	9.03	−0.52	6.18	11.76	8.62
P_E (HP)	Cal.	41,485	44,621	52,870	51,610	20,559	12,523	23,581	26,172
	Exp.	39,855	44,177	51,651	51,244	20,401	12,547	22,397	25,735
	Diff. (%)	4.09	1.01	2.36	0.71	0.77	−0.19	5.29	1.70

hypothesis of Prohaska (1966), i.e., the resistance coefficient may not be linear due to the waves generating from bulbous bow even in low-speed region ($F_N \approx 0.12$). In the case of twin-skeg ships, the value of the form factor is lower compared to single-skeg ships.

The computational values of C_{TM} are smaller than those of the model test except 319K VLCC. This is deemed to be due to the fixed model of non-trimming condition. Note that FuSS has wetted transom, whereas FiHS and FuMS have dry transoms as described in Table 2. In the case of the free model condition like the model test, the magnitudes of C_{TM} will become larger than those in the fixed model of non-trimming condition due to the increased transom immersion and the trimmed by stem. As a result of the smaller computational prediction of C_{TM}, the magnitudes of C_R become smaller compared to the results of the model test. In particular, it shows negative (−) values in the case of 172K BC and 150K/216K LNGC.

To know the trimming effect, the computation in the towing condition with the free-surface model is performed at the trimming condition for a 150K LNGC. The trim magnitudes are obtained from the experiment. Fig. 17 presents the sinkage ($\sigma = (\Delta T_{FP} + \Delta T_{AP})/L_{PP}F_N^2$) and trim coefficient ($\tau = (\Delta T_{FP} - \Delta T_{AP})/L_{PP}F_N^2$) obtained from the experiments for the various types of ships, where $\Delta T_{FP(AP)}$ is the draft difference between FP (forward perpendicular) [or AP (after perpendicular)] and midhip. The positive values of σ and τ mean that the model ship is sunken and trimmed by stem, respectively. All the objective ship models have positive values in σ and τ. The magnitudes of σ and τ increase as the hull form becomes fuller. The computational prediction of C_{TM} of 150K LNGC is 3.622×10^{-3} in the trimming condition, which is larger than 0.093×10^{-3} compared to that in fixed model of non-trimming condition. And C_R becomes positive (+) value of 0.026×10^{-3}. At any rate, the negative vale of C_R is unreasonable even if the model is at the non-trimming fixed condition. That is one of the reasons why the CFD-model test correlation coefficient (ΔC_{FM}) is introduced. As mentioned in Eq. (18), ΔC_{FM} is introduced to correct the difference of the total resistance coefficient between the experiments and the calculations. Fig. 18 presents the relationship between ΔC_{FM} and fullness parameter.

Note that the wide error range of C_R is due to the small magnitude itself. The C_R portions of C_{TM} are 5.16–6.84%, 1.46–1.48%, and 1.69–2.55% for HiFS, FuSS, and FuMS, respectively. In the respect of hull-form design, it will be reasonable way to reduce C_R for HiFS, whereas to increase propulsion efficiency for FuSS.

A noteworthy point here is that the results of the model test of 150K LNGC indicate that the form factor has a greater value than in the numerical prediction as in the FiHS, and the value of the residual resistance coefficient is smaller as in the FuSS.

The difference between the computational and the experimental prediction of P_E is −0.19% to 5.29%. Note that computational predictions of C_{TM} are lower than those obtained from the model tests due to the lower predictions of $(1+k)$ and C_R for the cases of FiHS and FuMS. These lower computational predictions are compensated for the predictions of C_{TS} (or P_E) by introducing the higher values of ΔC_{FM} than those of ΔC_F.

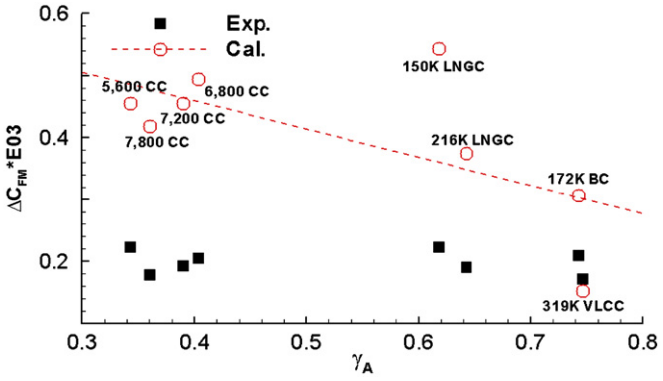

Fig. 18. Relationship between ΔC_{FM} and fullness parameter.

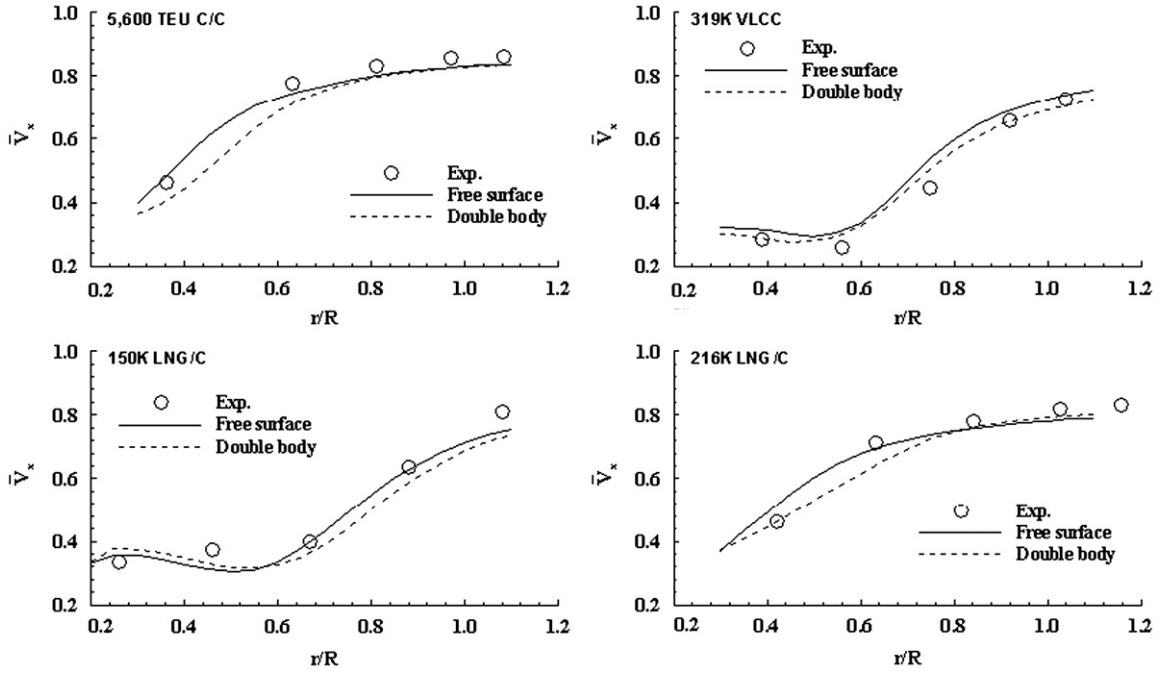

Fig. 19. Circumferentially averaged axial velocity on the propeller plane.

6.5. Propulsion characteristics

The computational predictions of $TF(=R_{VM}^{SP}-T_M)$ are lower than the experimental predictions except FuSS since the computational values of the viscous resistance in self-propulsion conditions (R_{VM}^{SP}) are also lower than the experimental values as discussed in Section 6.4. Note that the values of n_M, T_M and Q_M are affected by the free surface, whereas TF (or FD) not, since TF (or FD) is the difference of the viscous force between the model and the ship scale as expressed in Eq. (24). The magnitude of n_M is obtained from

$$n_M = \frac{V_M(1-w_M)}{J_M D_M} \tag{52}$$

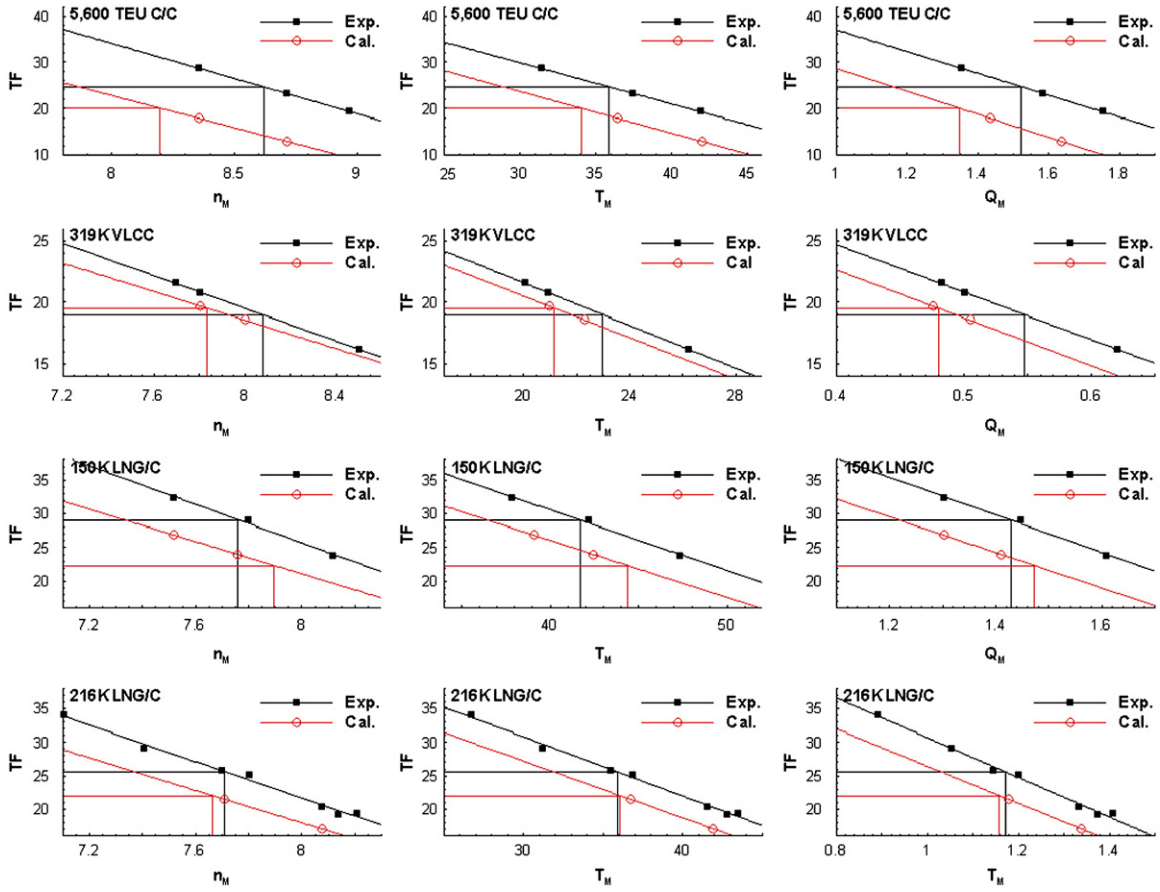

Fig. 20. Procedure to obtain a self-propulsion point for various types of commercial ships.

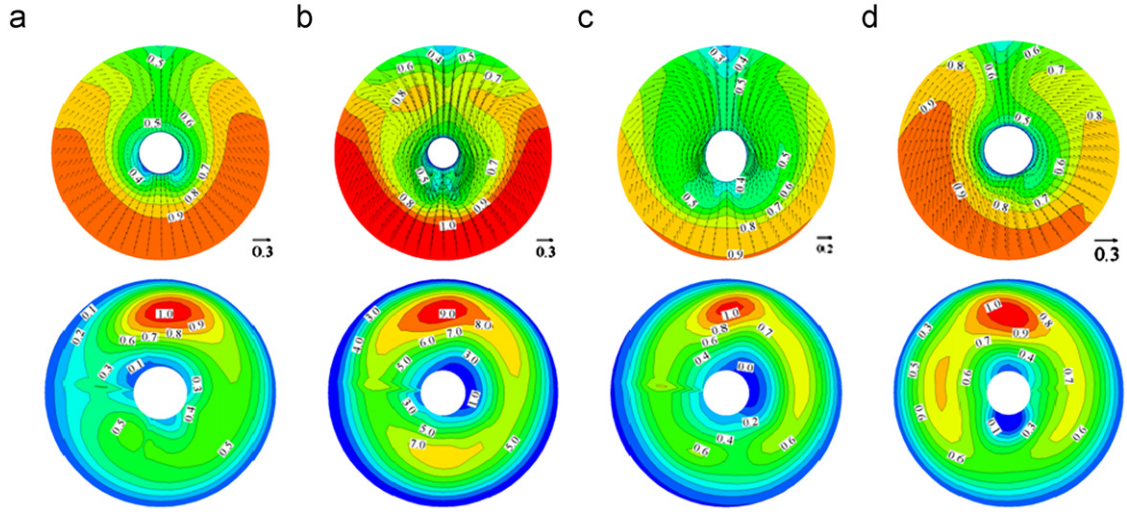

Fig. 21. Characteristics of effective velocity and thrust distribution function on the control plane: (a) 5600 CC, n_M=8.36 rps; (b) 319K VLCC, n_M=8.00 rps; (c) 150K LNGC, n_M=7.76 rps and (d) 216K LNGC (starboard), n_M=7.71 rps.

Table 12
Summary of self-propulsion factors and speed performances for various types of commercial ships.

		5600 CC	6800 CC	7200 CC	7800 CC	319K VLCC	172K BC	150K LNGC	216K LNGC
J_M	Cal.	0.778	0.669	0.687	0.727	0.368	0.433	0.538	0.724
	Exp.	0.796	0.691	0.711	0.751	0.359	0.393	0.549	0.733
	Diff. (%)	−2.26	−3.18	−3.38	−3.20	2.51	10.18	−2.00	−1.23
t	Cal.	0.168	0.172	0.185	0.163	0.210	0.205	0.192	0.228
	Exp.	0.176	0.177	0.180	0.182	0.256	0.230	0.209	0.240
	Diff. (%)	−4.55	−2.82	2.78	−10.44	−17.97	−10.87	−8.13	−5.00
w_M	Cal.	0.255	0.295	0.280	0.258	0.462	0.399	0.402	0.331
	Exp.	0.238	0.272	0.255	0.233	0.475	0.455	0.390	0.323
	Diff. (%)	7.14	8.46	9.80	10.73	−2.74	−12.31	3.08	2.48
w_S	Cal.	0.236	0.263	0.258	0.235	0.350	0.325	0.336	0.303
	Exp.	0.227	0.246	0.238	0.228	0.382	0.362	0.323	0.302
	Diff. (%)	3.96	6.91	8.40	3.07	−8.38	−10.22	4.02	0.33
η_H	Cal.	1.089	1.123	1.098	1.094	1.216	1.179	1.218	1.108
	Exp.	1.066	1.091	1.076	1.059	1.203	1.206	1.168	1.089
	Diff. (%)	2.16	2.93	2.04	3.31	1.08	−2.24	4.28	1.74
η_R	Cal.	1.050	1.053	1.043	1.041	1.071	1.072	1.038	1.029
	Exp.	0.991	1.006	0.999	0.982	1.014	1.040	1.011	1.016
	Diff. (%)	5.95	4.67	4.40	6.01	5.62	3.08	2.67	1.28
η_O	Cal.	0.696	0.645	0.659	0.668	0.577	0.587	0.629	0.683
	Exp.	0.694	0.644	0.657	0.660	0.555	0.573	0.642	0.684
	Diff. (%)	0.29	0.16	0.30	1.21	3.96	2.44	−2.02	−0.15
η_D	Cal.	0.796	0.763	0.753	0.760	0.748	0.741	0.794	0.778
	Exp.	0.732	0.707	0.705	0.687	0.676	0.716	0.755	0.756
	Diff. (%)	8.74	7.92	6.81	10.63	10.65	3.49	5.17	2.91
n_S (RPM)	Cal.	80.24	91.45	89.69	87.36	74.59	86.17	83.15	75.17
	Exp.	81.69	93.77	92.65	89.72	75.11	84.26	82.52	75.17
	Diff. (%)	−1.78	−2.47	−3.19	−2.63	−0.69	2.27	0.76	0.00
P_{DS} (HP)	Cal.	52,117	58,481	70,212	67,908	27,485	16,900	29,699	33,640
	Exp.	54,429	62,492	73,301	74,616	30,157	17,513	29,650	34,038
	Diff. (%)	−4.25	−6.42	−4.21	−8.99	−8.86	−3.50	0.17	−1.17

So, the magnitude of n_M is considered to be proportional to that of inflow velocity on the propeller plane, and those of T_M and Q_M are also proportional to that of n_M. Fig. 19 compares the circumferentially averaged axial velocities on the propeller plane between the free surface and double-body model. The inflow velocity on the propeller plane is increased due to the wave effect. As a result, the computational values of n_M, T_M and Q_M obtained from the double-body model are expected to be under-predicted when compared to those of the free-surface model as shown in Fig. 20. Fig. 20 presents the process to obtain the self-propulsion points of the various types of ships.

Fig. 21 refers to the effective velocity that flows into the propeller plane and the thrust distribution function. The effective velocity indicates the difference between the incoming velocity into the propeller plane and the propeller induced velocity. The magnitude of the thrust distribution function is smaller in the 2nd quadrant where the rotating direction of the propeller and the secondary flow are the same. The magnitude in the 1st quadrant is larger where the direction of the secondary flow is opposite. In the case of FuSS, this occurs across the entire the 1st quadrant. The high magnitude in the upper part of the propeller plane is due to the low velocity region near the ship. And the magnitude is of high in the 3rd and the 4th quadrant as well and this is due to the low axial velocity influenced by the stern hull form. In the case of twin-skeg ship, the magnitude is higher in the inner section of the skeg. This is due to the secondary flow in the opposite direction of the propeller's rotation in the inner area.

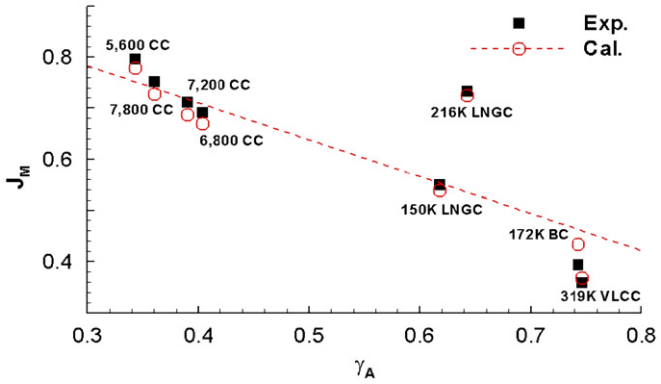

Fig. 22. Relationship between advance ratio and fullness parameter.

The speed performances including the self-propulsion factors are summarized in Table 12.

Fig. 22 indicates the relation between J_M and γ_A. The value of J_M ($=V_A/nD$, V_A: the incoming velocity into the propeller plane) decreases as the hull form becomes fuller. In the case of single-skeg ship, the trend of the experimental and the computational predictions with respect to γ_A is nearly same. In the case of twin-skeg ship, the value of J_M is higher.

Fig. 23 presents the relationship between self-propulsion factors (t, w_S) and γ_A. As the hull form becomes fuller, the

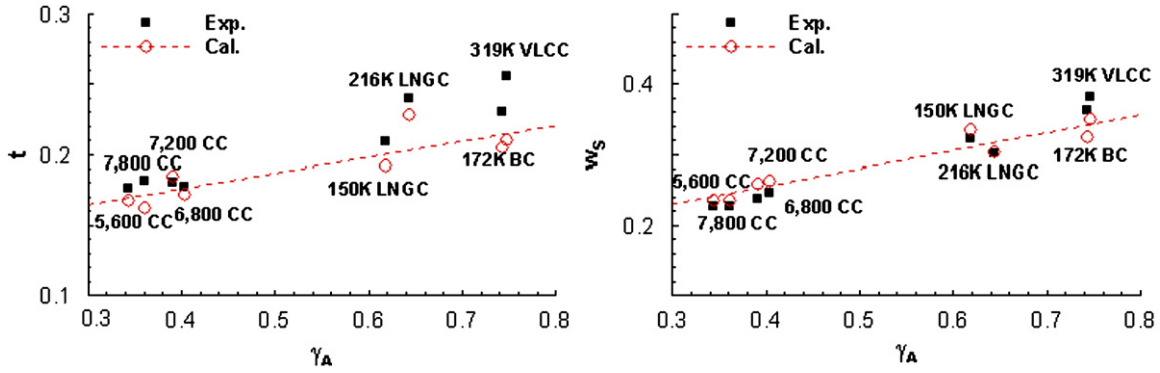

Fig. 23. Relationship between self-propulsion factor and fullness parameter.

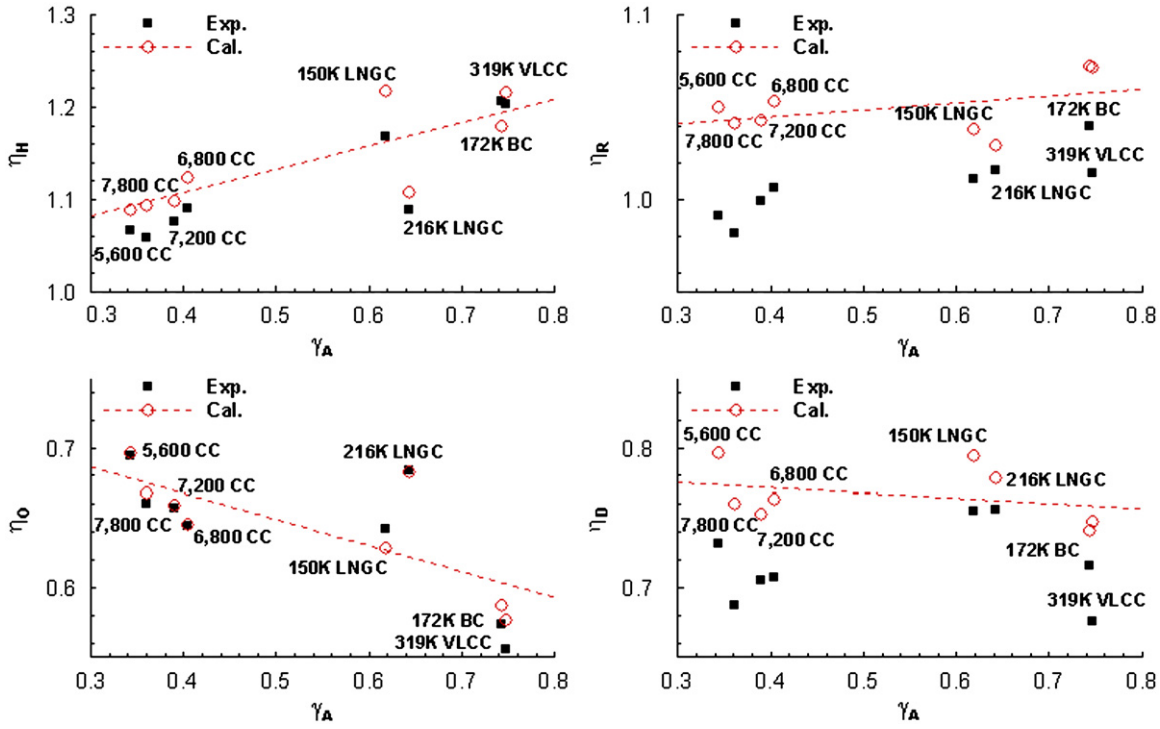

Fig. 24. Relationship between various efficiencies and fullness parameter.

values of t and w_S tend to become larger. Note that the slope of w_S is greater than that of t.

Fig. 24 shows the relationship between various efficiencies and γ_A. As the hull form becomes fuller, the values of η_H and η_R tend to become larger and η_O smaller. The value of η_H increases with γ_A since the slope of w_S has a greater impact. The decline in η_O can be easily referred from the trend of J_M. The computational predictions of η_R are all larger than those of the model tests (2.7–6.0%) because Q_M does not include free-surface effect. η_D does not exhibit trend with regard to γ_A. The computational predictions are larger than those of the model tests by 3.5–10.7%.

6.3. Propeller rotative speed and delivered power

The differences between the computational and the experimental predictions are n_S stands -3.19% to 2.27% and P_{DS} -8.99% to 0.17%. These indicate that the computational predictions can be applied to the hull-form design in the initial stages although there are still rooms to boost accuracy, especially, in the cases of larger size of container carrier and VLCC.

7. Conclusions

This study employed computational methods to examine the resistance and propulsion characteristics of eight commercial ships. The computational predictions reveal similar tendencies with the experimental approach, save for minor differences. Such differences, however, suggest that there is potential to apply the computational method to predicting speed performances in the initial hull-form design stage. Further research is required to enhance accuracy and to actually tap into the approach during the designing phase. Trimming, propeller geometry and free surface in self-propulsion calculation are elements to consider for greater precision. Another point to consider is whether the differences in

speed performance resulting from the slight variations of the hull form and propellers are predictable.

References

Chao, K.Y., 2005. Numerical propulsion simulation for the KCS container ship. In: Proceedings of CFD Workshop 2005, Tokyo, Japan.

Choi, J.E., Kim, J.H., Lee, H.G., Choi, B.J., Lee, D.H., 2009. Computational predictions of ship-speed performance. Journal of Maritime Science and Technology 14 (3), 322–333.

Choi, J.K., Kinnas, S.A., 2001. Prediction of non-axisymmetric effective wake by a three-dimensional Euler solver. Journal of Ship Research 45, 13–33.

Choi, J.K., Kinnas, S.A., 2003. Prediction of unsteady effective wake by a Euler solver/vortex-lattice coupled method. Journal of Ship Research 47, 131–144.

Fluent 6.3 User's Guide, 2008. Fluent Inc.

Gorski, J.J., Coleman, R.M., 2005. Computations of the KVLCC2M tanker under yawed conditions. In: Proceedings of CFD Workshop 2005, Tokyo, Japan.

Gridgen User Manual Version 15, 2003. Pointwise Inc.

Hino, T., 2006. CFD-bsed estimation of propulsive performance in ship design. In: Proceedings of the 26th Symposium on Naval Hydrodynamics.

Hino, T. (Ed.), 2005. In: Proceedings of CFD Workshop 2005, Tokyo, Japan.

Kawamura, T., Miyata, H., Mashimo, K., 1997. Numerical simulation of the flow about self-propelling tanker model. Journal of Maritime Science and Technology 2, 245–256.

Kim, J., Park, I.R., Kim, K.S., Van, S.H., 2005. RANS computation of turbulent free surface flow around a self propelled KLNG carrier (in Korean). Journal of the Society of Naval Architects of Korea 42, 583–592.

Kodama, Y. (Ed.), 1994. In: Proceedings of CFD Workshop 1994, Tokyo, Japan.

Lee, D.H., Lee, H.G., 2004. Prediction of rudder cavitation considering propeller and hull effects. In: Proceedings of the Fourth Conference for New Ship and Marine Technology.

Leonard, B.P., Mokhtari, S., 1990. ULTRA-SHARP nonoscillatory convection schemes for high-speed steady multidimensional flow. NASA TM 1-2568 (ICOMP-90-12), NASA Lewis Research Center.

Lindgren, H., Aucher, M., Bowen, B.S., Gross, A., Minssas, K.J., Muntjewerf, J.J., Tamura. K., Wermter, R., 1978. Report of the Performance Committee. In: Proceedings of the 15th International Towing Tank Conference.

Lübke, L.O., 2005. Numerical simulation of the flow around a propelled KCS container ship. In: Proceedings of CFD Workshop 2005, Tokyo, Japan.

Park, I.R., Kim, J., Van, S.H., 2004. Analysis of resistance performance of modern commercial ship in hull form using a level-set method (in Korean). Journal of the Society of Naval Architects of Korea 41 (2), 79–89.

Patankar, S.V., Spalding, D.B., 1972. A calculation procedure for heat, mass and momentum transfer in three-dimensional parabolic flows. International Journal of Heat and Mass Transfer (15), 1787–1806.

Prohaska, C., 1966. A simple method for the elevation of the form factor and low speed wave resistance, Report of the Performance Committee. In: Proceedings of the 11th International Towing Tank Conference.

Report of the Performance Committee, 2002. In: Proceedings of the 23rd ITTC.

Sasajima, H., Tanaka, I., 1974. Form effects on viscous resistance and their estimation for full ships. In: Proceedings of the 10th Symposium on Naval Hydrodynamics, pp. 122–128.

Stenson, R., Boss, N., van den Berg, W., Garcia-Gromez, A., Gulbrandsen, B., Hadjimikhalev, V., Jensen, G., Miranda, S., Shen, O.-X., Tsutsumi, T., 1996. Report of the Performance Committee. In: Proceedings of the 21st International Towing Tank Conference.

Stern, F., Kim, H.T., Chen, H.C., 1988. A viscous-flow approach to the computation of propeller-hull interaction. Journal of Ship Research 32 (4), 246–262.

Tahara, Y., Wilson, R.V., Carrica, P.M., Stern, F., 2006. RANS simulation of a container ship using a single-phase level-set method with overset grids and the prognosis for extension to a self-propulsion simulator. Journal of Maritime Science and Technology 11, 209–228.

Tobak, M., Peake, S.J., 1982. Topology of three-dimensional separated flows. Annual Review of Fluid Mechanics 14, 61–85.

Wilson, R.V., Shao, J., Stern, F., 2004. Discussion: criticisms of the "correction factor" verification method [1]. Journal of Fluids Engineering 126, 704–706.

Xing, T., Stern, F., 2008. Factors of safety for Richardson extrapolation for industrial applications. IIHR Technical Report 466.

Yamano, T., Ikebuchi, T., Funeno, I., 2000. On forward-oriented wave breaking just behind a transom stern. Journal of the Society of Naval Architects of Japan. 187, 25–32.